# Aerosol mapping over land with imaging spectroscopy using spectral autocorrelation

S. Bojinski [a,b], D. Schläpfer [a], M. Schaepman [a,*], J. Keller [b], and K. Itten [a]

[a] *Remote Sensing Laboratories, Department of Geography, University of Zürich, Winterthurerstrasse 190, CH-8057 Zürich, Switzerland*

[b] *Laboratory for Atmospheric Chemistry, Paul Scherrer Institut, CH-5232 Villigen-PSI, Switzerland*

**Abstract**

A new method for aerosol retrieval over land is proposed that makes explicit use of the contiguous, high-resolution spectral coverage of imaging spectrometers. The method is labelled Aerosol Retrieval by Interrelated Abundances (ARIA) and is based on unmixing of the short-wave infrared sensor signal by region-specific endmembers, assuming low aerosol radiative influence in this spectral region. Derived endmember abundances are transferred to the visible part of the spectrum in order to approximate surface reflectance where aerosol influence is generally strongest. Spectral autocorrelation of surface spectra is a precondition for ARIA and demonstrated using a reference spectrum database. The re-mixed surface reflectance is used as input quantity for the inversion of aerosol optical depth $\tau_a$ at 0.55 $\mu$m wavelength on a pixel basis. Except for the choice of endmembers and the atmospheric vertical profile, no *a priori* assumptions on the image scene are required. The potential of the presented method for aerosol retrieval is demonstrated for an AVIRIS

scene, collected in California in 2000. Comparisons with existing aerosol retrieval methods showed encouraging results in terms of achieved spatial smoothness and degree of uncertainty of aerosol optical depth across the scene.

*Key words:* imaging spectroscopy, aerosols, spectrum database, spectral autocorrelation

## 1 Introduction

In the Earth's atmosphere, natural and anthropogenic sources give rise to highly variable geographical and seasonal aerosol distributions, which are largely confined to the troposphere. Aerosols affect the atmospheric radiative transfer of sunlight directly due to scattering and absorption of radiation at particles, and indirectly by influencing the formation of clouds. Owing to the high spatial variability of aerosols, continuous *in situ* monitoring from ground-based instrument networks (e.g., ground-based Sun photometry) is insufficiently representative for both regional and global applications, and calls for imaging remote sensing techniques. Over both dark water and dark vegetation areas on the Earth's surface, the presence of aerosols generally brightens these pixels at the satellite or aircraft sensor level, which is described by the aerosol effect $\rho_a$. This effect is most often exploited for the retrieval of aerosol parameters. The aerosol effect is defined by the difference of apparent reflectance at sensor level $\rho_{app}$, reduced by the apparent reflectance that would be measured if no aerosol were present for the same measurement situa-

* Corresponding author; phone +31 317 47 46 45; fax +31 317 41 90 00
*Email address:* Michael.Schaepman@wur.nl (M. Schaepman).
*URL:* http://www.geo-informatie.nl (M. Schaepman).

tion. Apparent reflectance is total upwelling radiance, normalized by the total downwelling irradiance, both evaluated at the sensor level.

The earliest studies on aerosol remote sensing from satellites used Landsat-1 data in single VIS bands for mapping dust over the ocean (Fraser, 1976). Gordon (1978) made first steps in the correction of ocean color measurements for aerosol influence using two spectral bands over the oceans, and refined the algorithm for combined ocean colour and aerosol retrieval from SeaWiFS imagery (Gordon and Wang, 1994). Tanré et al. (1997) used bands in a spectral range between 0.55 and 2.13 $\mu$m of the MODIS airborne simulator and a look-up table approach to derive aerosol properties over the ocean. Unless models or *in situ* measurements exist that account for the effects of wind speed and suspended matter (Gordon and Wang, 1994), water bodies are approximated to reflect $0-1$ % of the downwelling irradiance above its surface in the NIR. First studies on the retrieval of aerosol properties from satellite sensor data over land, which is generally more complex, were aimed at atmospheric correction (Tanré et al., 1983), but soon focused equally on aerosol mapping (Kaufman and Sendra, 1988), making use of dark vegetation targets in the VIS. Dark vegetation is mostly approximated by $2-3$ % reflectance in the red VIS (Richter, 1996). In imagery uncorrected for the atmospheric signal, dark vegetation can be identified by thresholding of the atmospherically resistant vegetation index (ARVI) (Kaufman and Tanré, 1992). With the advent of space-borne sensors that have the specific capability for aerosol retrieval (e.g. MODIS), the dark target approach has been refined over land. The method proposed by Kaufman et al. (1997), hereinafter referred to as "band ratio method", is based on an empirical relationship between SWIR reflectance at $\lambda = 2.1$ $\mu$m and visible reflectances at $\lambda = 0.49$ $\mu$m and $\lambda = 0.66$ $\mu$m for

a large variety of natural surfaces. It assumes a weak aerosol effect in the infrared, which holds except for very large dustlike or sea-salt particles. In contrast to single-view instruments, sensors with multi-angle view capability have also been used for the retrieval of atmospheric aerosol properties, such as for ATSR-2 (Veefkind et al., 2000), MISR (Martonchik et al., 1998), and POLDER (Leroy et al., 1997), but are not further considered in this study. In recent years, space-borne imaging spectroscopy has become an important means to characterize aerosols on both global and regional scales (King et al., 1992; Tanré et al., 1997; Kaufman et al., 2002). Airborne spectral imagers, such as AVIRIS (Green et al., 1998), with continuous spectral coverage between 0.4 and 2.5 $\mu$m in hundreds of bands, and ground sampling distances of the order 10 m have also been used for the retrieval of aerosol parameters: Isakov et al. (1996) infer aerosol optical depth from contrast reduction of uniform artificial land surface targets with high reflectance difference, due to atmospheric blurring. In turn, imaging spectroscopy of the Earth's surface, often requires accurate atmospheric correction of spectral images, and therefore knowledge of the aerosol radiative effect (Gordon, 1978; Chomko and Gordon, 1998; Gao et al., 2000).

In this paper, a new method for aerosol retrieval over land is proposed that makes explicit use of the contiguous and high-resolution spectral coverage of imaging spectrometers. It is based on unmixing of the short-wave infrared sensor signal by appropriate endmembers, assuming low aerosol radiative influence in this spectral region. Endmember abundances, that are obtained from the unmixing process, are then applied to the visible part of the endmembers in order to approximate surface reflectance in this spectral region where aerosol influence is generally strongest. The re-mixed surface reflectance is used as in-

put quantity for numerical inversion of aerosol optical depth. The final goal of the method consists of mapping regional distributions of aerosol optical depth, integrated over the atmospheric column. Imagery from the Airborne Visible Infrared Imaging Spectrometer (AVIRIS) described by Green et al. (1998) is used as test data. This study focuses on the derivation and description of the new method. A cross-comparison to existing methods for aerosol retrieval with optical imaging spectrometers is performed, while absolute validation data for aerosol optical depth has not been available.

The following terminology is used for spectral wavelength ranges throughout this paper: visible (VIS) range denotes wavelengths $\lambda$ between 0.4 and 0.7 $\mu$m, near infrared (NIR) means $\lambda = 0.7 - 1.0$ $\mu$m, and short-wave infrared (SWIR) refers to wavelengths between 1.0 and 2.5 $\mu$m. From the SWIR range, the two wavelength regions between 1.4 and 1.8 $\mu$m and $1.8 - 2.5$ $\mu$m are referred to as SWIR1 and SWIR2, respectively.

## 2 New method for aerosol retrieval over land using imaging spectroscopy

### *2.1 Basic principle*

A new method for the retrieval of aerosol parameters from imaging spectrometer data over land is proposed. Unlike the dark target and band ratio methods, which use a small number of spectral bands for the approximation of land surface reflectance $\rho_s$ in an image pixel, the Aerosol Retrieval by Interrelated Abundances (ARIA) method is based on unmixing of the spectrally continuous sensor signal in the SWIR range, using the derived abundances to re-mix

the VIS surface reflectance, and subsequent inversion of aerosol parameters with look-up tables.

(Insert figure 1 about here)

As illustrated in figure 1, continuous spectral coverage of $\rho_s$(VIS) is thus achieved. Unmixing of the sensor spectrum $\rho_{app}$ in the SWIR (light grey, upper panel) uses *a priori* defined land surface reflectance endmembers $e_i$ (lower panel), assuming a low aerosol effect in the SWIR range. $\rho_{app}$ then reads for a linear combination of endmembers $e_i$

$$\rho_{app}(\text{SWIR}) = \sum_i a_i e_i(\text{SWIR}) \ . \tag{1}$$

Thus obtained abundances $a_i$ are interrelated between VIS and SWIR spectral ranges, if spectral autocorrelation of surface reflectances is given. In this case, re-mixing of the surface reflectance spectrum $\rho_s$(VIS) can be carried out by applying the abundances $a_i$ to the same set of endmembers as employed for unmixing, such that

$$\rho_s(\text{VIS}) = \sum_i a_i e_i(\text{VIS}) \ . \tag{2}$$

Once $\rho_s$(VIS) is obtained, radiative transfer forward modelling with look-up tables calculated for a variation of aerosol parameters and terrain heights is performed, and the best fit of $\rho_{app}^{sim}$ to the measured image spectrum $\rho_{app}$(VIS) is sought. Figure 2 illustrates this procedure for different modelled columnar aerosol optical depths $\tau_a(0.55\mu\text{m})$ for a maritime aerosol model as defined by Shettle and Fenn (1979). $\tau_a(\lambda)$ is always evaluated for $\lambda = 0.55$ $\mu$m in the following, and henceforth denoted as $\tau_a$. The best fit curve is determined by

minimizing the cost function $\epsilon_{\tau_a}$

$$\epsilon_{\tau_a} = \frac{1}{n}\sqrt{\sum_{j=1}^{n}(\rho_{app}^{sim}(\lambda_j) - \rho_{app}(\lambda_j))^2} \tag{3}$$

with $n$ denoting the number of spectral bands.

(Insert figure 2 about here.)

With a minimum $\epsilon_{\tau_a}$, $\tau_a^{best}$ is found, which represents the retrieved aerosol parameter. It depends on approximated surface reflectance $\rho_s$(VIS), measured $\rho_{app}$ at the sensor, and the atmospheric model that is used in the look-up table forward calculations.

### *2.2 Implementation of method*

(Insert figure 3 about here.)

Based on the described basic principle, the implementation of the ARIA method is depicted in figure 3.

*Step (0):* As the spectral image scene over land generally contains variable topography, orthorectification is performed. A digital terrain model at approximately the same spatial resolution as the image data is needed for that purpose.

*Step (1):* Spectral endmembers can be conceived as the eigenvectors that describe each pixel spectrum in an image scene without atmospheric disturbances (for a rigorous definition of the endmember concept, consult e.g. Richards and Jia (1999)). Unfortunately, this concept is approximative, as real scenes are not really composed of small number of distinct pure materials, nor are pixel

spectra exact linear combinations of the spectra of these materials. In this context, no image-based automated endmember selection algorithm that is insensitive to atmospheric perturbations could be identified in the literature. In many studies of land cover analyses using spectral unmixing (Roberts et al., 1998; Asner and Lobell, 2000), specific spectrum databases are used, that are adapted to regional conditions. In the proposed method, a reference spectrum database (Bojinski et al., 2003) provides a set of surface spectra measured in nadir direction, that fulfil the following conditions: (a) measured in the area of the image scene in question, and (b) measured in a season comparable to the time of image acquisition. Significant autocorrelation of the selection of surface spectra between the VIS and the SWIR wavelength ranges is a precondition (see section 4). Endmember spectra can then be obtained by averaging the subset of surface spectra being measured on identical or similar land cover types. It depends on the land cover abundances in the image scene which of these endmembers are chosen for the following steps. For example, in case of a predominantly rural image, two endmembers are suggested: vegetation and soil. It must be noted that spectral shapes that are representative for surface types in the scene area are required, which are ideally, but not necessarily measured during overflight. Only surface/object-inherent spectral properties are required for the method, not the actual ground spectra in absolute reflectance units (cf. steps (3) and (4)).

*Step (2):* With the spectral angle mapper (SAM) algorithm (Richards and Jia, 1999), image pixels are identified that bear sufficient similarity to one of the used endmember spectra $e_i$, in the sense that a pixel belongs to class $c$ by the

condition

$$c = \begin{cases} i & : \quad \min\left(\arccos\left(\frac{\rho_{app,j} e_{i,j}}{|\rho_{app,j}||e_{i,j}|}\right)\right) \leq 0.15 \\ 0 & : \quad \text{else,} \end{cases} \tag{4}$$

using the spectral bands $j$, which were chosen at 0.66, 0.87, 1.04, 1.66, and 2.10 $\mu$m. This band selection is small enough to enable fast image classification, and at the same time roughly covers the spectral range of interest. "0" in equation (4) denotes "unclassified". This implies that the pixel spectrum $\rho_{app,j}$ cannot be properly modelled by the chosen endmembers, probably due to a highly different surface cover measured in the pixel area. As endmembers were chosen according to the predominant surface covers in step (1), good coverage of the image by successfully classified pixels ($c$ not zero) is expected. The SAM is considered fairly robust towards atmospheric perturbation of the sensor signal, and therefore the algorithm of choice. As the selection of endmembers is a very general one in terms of land covers, it is not expected that classified pixels are purely covered by the respective surface cover. This is important to note for the following processing step.

*Step (3) and (4):* In all successfully classified pixels, the SWIR range of the sensor signal is used for the unmixing procedure, employing the singular value decomposition technique (Press et al., 1992), and all endmembers used in the classification process. Even though derived abundances $a_i$ do not necessarily represent actual land cover abundances in the pixel area, they are a measure for the composition of the SWIR sensor spectrum, as expressed by the selected endmembers. Significant autocorrelation of natural surface spectra suggests that the $a_i$ be interrelated between SWIR and VIS for certain spectral bands and accuracy limits. Interrelation means that the $a_i$ as derived from the SWIR

can equally be used in the VIS part of the spectrum for re-mixing, because the spectral values have shown significant correlation. For unmixing, the use of all spectral bands in the preliminary range between 1.5 and 2.5 $\mu$m is suggested, provided the atmospheric transmission is larger than 0.85 (for a simulated maritime aerosol model and $\tau_a = 0.22$). This constraint prevents absorption features from atmospheric gases (water vapour, carbon dioxide) affecting the SWIR spectrum. However,the surface spectra autocorrelation analysis defines the exact SWIR unmixing range within the preliminary range.

Surface BRDF characteristics are not expected to adversely affect the unmixing/re-mixing procedure, which is carried out with spectra measured at nadir, provided that BRDF is independent of wavelength.

The assumption of low aerosol effect ($\rho_a \leq 0.004$) in the SWIR is considered true for $\tau_a \leq 0.25$ in the sense that $\rho_{app}(\mathrm{SWIR})$ can be taken as measured on the sensor level for unmixing, provided that $\overline{\rho_{app}(\mathrm{SWIR})} < 0.15$ (Kaufman et al., 1997). For $\tau_a > 0.25$, the aerosol effect on $\rho_{app}(\mathrm{SWIR})$ can no longer be considered weak in general. In this case, a posteriori correction of the aerosol effect in the SWIR is needed and a second iteration of the procedure based on the result from step (8) (described below) is required. In this paper, the cases where $\tau_a > 0.25$ are not considered further. Re-mixing of $\rho_s(\mathrm{VIS})$, as described in equation (2), is performed in the spectral range between 0.42 and 0.50 $\mu$m, where the scattering influence of aerosol is generally strongest (step (4)).

*Step (5):* Upward-calculating the approximated ground spectrum in VIS bands for aerosol parameter variations is carried out numerically by means of pre-calculated look-up tables. The MODTRAN 4.0 radiative transfer code (Berk et al., 1989) was used for that purpose, which assumes a spatially uniformly

layered atmosphere, approximately plane-parallel on a regional scale, with the following set of parameters (values in parentheses denote incremental steps of the respective parameters):

- Nadir sensor viewing direction
- Sun zenith, azimuth, day of year, sensor altitude: adapted to test dataset
- Columnar water vapour 1.41 g/cm$^2$ and ozone 7.36 g/cm$^2$
- 15 cm$^{-1}$ resolution absorption band model
- Variation in terrain height $h$: adapted to test area terrain variation in 1.0 km increments
- Variation in spectrally uniform $\rho_s$: 0.0(0.02)0.2, 0.23, 0.26, 0.3(0.05)0.5
- Variation in horizontal visibility $V$ [km]: 6.0(0.5)10.0, 11.0(1.0)15.0, 17.0, 19.0, 21.0, 23.0 26.0, 30.0, 35.0, 40.0, 45.0, 55.0, 65.0, 80.0, 100.0, 120.0 (corresponds to variation of tau for $h$=0.0 km: $1.004 - 0.076$)
- Aerosol models in the boundary layer: maritime, rural, urban (separate look-up tables)
- Wavelength range: $0.37 - 0.80$ $\mu$m

For the numerical inversion of aerosol optical depth, the look-up table spans in $\rho_s$ and $\tau_a$ dimensions, for the urban, rural, and maritime aerosol models. This choice of parameters has been made according to a study by Tanré et al. (1997) for look-up table-based aerosol retrieval with the MODIS instrument. Each combination of $\rho_s$, $\tau_a$, and an aerosol model results in a simulated $\rho_{app}^{sim}$ at the sensor level (see figure 2).

*Step (6):* The procedure to find the best fitting simulated at-sensor spectrum is based on minimizing the cost function in equation (3). If $\rho_{app}$ exceeds the set of simulated curves in more than one used band, the inversion is cancelled for this particular pixel. In any other case, for maritime, urban, and rural aerosol

models, the aerosol optical depth $\tau_a$ for each candidate pixel is obtained.

*Step (7):* Uncertainty in the retrieved aerosol parameter $\Delta\tau_a$ is expressed by equation (7). Pixels are excluded from further processing if the normalized uncertainty $\Delta\tau_a/\tau_a$ exceeds a threshold value, which is chosen at 0.75. This value represents a reasonable trade-off between the number of useable pixels and the accuracy of the ARIA method.

*Step (8):* The raw aerosol optical depth map is being averaged on a grid with approximate cell size 200-300 m, considered an appropriate scaling distance for the variation of aerosols on a local basis in very general terms. Averaging leads to a spatially more continuous spatial distribution of aerosol optical depth. Grid areas containing no appropriate pixels are left blank.

### *2.3 Error calculation*

The uncertainty in retrieved aerosol optical depth $\Delta\tau_a$ is determined from estimates of the uncertainties $\Delta\rho_s$ (uncertainty of re-mixed surface reflectance) and $\Delta\rho_{app}$ (uncertainty of sensor measurement). From a correlation analysis of natural reflectance spectra in the VIS and SWIR ranges, as collected in the image scene area, $\Delta\rho_s(\lambda)$ has been determined for each VIS spectral band. $\Delta\rho_{app}$ is given by the calibration accuracy of the sensor. Uncertainties are then calculated as follows: maximum and minimum retrieved aerosol optical depths $\tau_a^{max}$ and $\tau_a^{min}$ are obtained as

$$\tau_a^{max} = f(\rho_s(\lambda) - \Delta\rho_s(\lambda), \rho_{app}(\lambda) + \Delta\rho_{app}(\lambda)) \text{ , and} \tag{5}$$

$$\tau_a^{min} = f(\rho_s(\lambda) + \Delta\rho_s(\lambda), \rho_{app}(\lambda) - \Delta\rho_{app}(\lambda)) \text{ ,} \tag{6}$$

following the described inversion procedure. Equation (5) describes the case when surface reflectance is underestimated by its uncertainty, with sensor signal being overestimated to the maximum. In the inversion fitting process, this combination results in maximum estimated $\tau_a$. The vice versa combination in equation (5) analogously leads to $\tau_a^{min}$.

Additionally, an error in inverted aerosol optical depth results from the quality of the apparent reflectance fit at sensor level, depending on assumed aerosol optical depth (cf. equation (3)). Here, the minimum deviation $\epsilon_{\tau_a}$ can be converted into an uncertainty $\Delta\tau_a^{\epsilon}$ by a linear interpolation within the set of apparent reflectance curves (cf. figure 2).

The maximum total uncertainty in $\tau_a$, $\Delta\tau_a$ is then calculated by the discrepancy between $\tau_a^{max}$, $\tau_a^{min}$, and $\tau_a^{best}$, and the addition of $\Delta\tau_a^{\epsilon}$:

$$\Delta\tau_a = \frac{1}{2}(|\tau_a^{max} - \tau_a^{best}| + |\tau_a^{min} - \tau_a^{best}|) + \Delta\tau_a^{\epsilon} \ . \tag{7}$$

$\tau_a \pm \Delta\tau_a$ can be determined for each image pixel that is considered as candidate for the ARIA method. A candidate pixel mask is obtained by applying a spectral angle classifier to the raw image, using above mentioned surface reflectance endmembers.

## 3 Imaging spectrometer data

Airborne image data from the AVIRIS onboard a modified U-2 aircraft are used in this study to test the ARIA method and compare it to existing methods. An east-west flight line was acquired on 16 September 2000 at 11.00 am local time, stretching from downtown Los Angeles westward to Point Mugu

near Oxnard, across a distance of 94.5 km. The north-south extension is 12.3 km, including the shoreline and the Santa Monica Mountains range (see figure 4). AVIRIS scans the surface in 224 spectral bands between 0.37 and 2.51 $\mu$m at a spectral resolution of 10 nm, maximum scan angle 15.6° at 20 km altitude above sea level, and a ground sampling distance of 20 m.

Green and Pavri (2001) state the calibration uncertainty in the AVIRIS 2000 sensor signal as $\Delta\rho_{app}(\lambda) = 0.038\rho_{app}(\lambda)$ for all bands, evaluated over a bright target ($\rho_s = 0.5$). Bands with centre wavelengths below 0.415 $\mu$m are not recommended for use due to low calibration confidence and high noise level (Green, pers. comm.). In this study, AVIRIS bands $6 - 224$ with centre wavelengths $0.42 - 2.51$ $\mu$m are considered.

(Insert figure 4 about here.)

The Los Angeles/Point Mugu AVIRIS flightline has been chosen as a useful testing ground for the ARIA method, because

- it has been acquired with the AVIRIS sensor in the year 2000 calibration state, with significantly lower noise in the VIS bands than in previous years (Green and Pavri, 2001),
- it is cloud-free,
- it includes different land cover types and strong topography, where aerosol retrieval method performances over land can be compared and are expected to vary.

The Sun geometry was 41° Sun zenith angle, and 135° Sun azimuth angle. Hence, the scene is Sun-illuminated from the south-east.

As exemplary test area, the "Topanga" scene has been used throughout the

analysis, as depicted in figure 4. A USGS digital elevation model with a spatial resolution of 10 m was necessary for orthorectification of the scene, carried out with a parametric approach by Schläpfer and Richter (2002). The terrain model reveals that the "Topanga" scene mainly contains mountainous areas of the Santa Monica Mountains to the north and west, mostly covered by chaparral and dry bushlands, with terrain heights varying between 0 and 703 m. Some patches of dark green vegetation could be identified at the valley bottoms. Bright bare soil can be identified mostly along cross-country roads and at creek mouths into the sea. Centre, east and south-east of the scene show urban areas, where brightness is roughly proportional to building density. The urban sprawl partly extends into hilly areas above the centre of the scene. A very bright beach before Santa Monica is visible, shoring the Pacific Ocean to the south-west. The injection of suspended sediments at creek mouths can be distinguished below the centre of the "Topanga" scene, brightening the mostly uniform ocean water.

As exemplary subscenes of the "Topanga" dataset, a valley covered almost entirely by vegetation and soil, not containing built-up areas ("Valley"), as well as an urban area containing significant amounts of vegetation cover ("Urban"), have been selected.

For the entire scene, a variety of aerosol types, such as rural, maritime, and urban, can be expected as predominantly occurring due to the proximity of respective sources. Therefore, these three aerosol models are used in this study for the inversion of aerosol optical depth. As a rough estimate, the latter is expected to vary roughly around 0.20 (cf. Seinfeld and Pandis (1998)) for a fairly clear day in the Los Angeles area, with possible fluctuations due to terrain elevation and proximity to aerosol sources in the urban Los Angeles area).

The 0.2 value for $\tau_a$ has also been confirmed from a preliminary atmospheric correction of the scene using the ATCOR4 program (Richter and Schläpfer, 2002). A uniform horizontal visibility $V = 40$ km (corresponding to columnar optical depth 0.20) and maritime and rural aerosol models yielded most appropriate atmospherically corrected ground spectra. Assuming a well-mixed aerosol in a 2 km thickness boundary layer, resulting in aerosol extinction coefficient $\sigma_{e,a} = 0.1$ km$^{-1}$, terrain height variations of 700 m as mentioned give rise to $\tau_a$ variations of around 0.07.

For spectral angle mapping (step (2) of ARIA), band numbers 33, 55, 73, 138, and 183 are used. The SWIR1 and SWIR2 spectral regions correspond to AVIRIS bands $124 - 144$ and $182 - 204$, respectively. The effect of varying zenith angle of the sensor viewing direction ($\pm$ 15.6°) on the sensor signal (due to increased optical path length) is considered negligible.

## 4 Autocorrelation analysis of surface spectra

The ARIA method is based on significant autocorrelation of natural surface spectra in the VIS and SWIR spectral regions. The degree of this autocorrelation is investigated based on data from a spectrum database that were measured in the area of the AVIRIS image.

Similar analyses have been carried previously: using low-altitude airborne spectral image data, a significant correlation between reflectances at 2.1 $\mu$m and reflectances at 0.49 and 0.66 $\mu$m, respectively, could be proven empirically (Kaufman et al., 1997) for several natural surface types (vegetation, soils, sand). Karnieli et al. (2001) showed a significant correlation between

bands at 0.645 and 1.6 $\mu$m for vegetation targets. In this analysis, correlation is investigated for spectral bands between 0.4 and 0.7 $\mu$m in the VIS, and the SWIR1 and SWIR2 regions, respectively.

A region-specific selection from the spectrum database SPECCHIO (Bojinski et al., 2003) yielded reflectance spectra from bare soil (35 spectra) and different vegetation types typical for chaparral (25 spectra). Averaged band correlations were calculated.

(Insert figure 5 about here.)

The results in figure 5 show panels with Pearson's correlation coefficient $r_{xy}$, pair-wise determined for bands $x$ and $y$. It represents a measure for the degree of association between the reflectance values in the respective bands. Considering the size of spectral ensembles and assuming normally distributed reflectance values, $r_{xy} > 0.5$ indicates statistically significant correlation (cf. Press et al. (1992, 636)). Panels (a) in figure 5 display the correlation matrices between VIS and SWIR1, panels (b) the same for VIS and SWIR2. For the spectral ensemble of soils, $r_{xy}$ above 0.90 is ubiquitous in the VIS/SWIR2 matrix, suggesting very good correlation of spectra. The same panel in the vegetation case shows overall less, but still significant correlation at around 0.70, but with a marked region of low values in the green trough region between 0.50 and 0.55 $\mu$m, and above 2.4 $\mu$m in the SWIR part. The dip in correlation in the green is also discernible in the VIS/SWIR1 plot, an overall smoother picture with correlation coefficients between 0.7 and 0.8. It is probably due to the strong variability of plant chlorophyll content, which is generally not reflected in the SWIR spectral range. For soils, correlation is much lower in the VIS/SWIR1 panel, with values tending to insignificance below 0.50 $\mu$m,

and increasing to about 0.8 for higher VIS wavelengths. From the observed autocorrelation levels, an unmixing SWIR range between 1.97 and 2.38 $\mu$m is chosen, well-correlated for both soils and vegetation in this spectral selection with the VIS range between 0.40 and 0.50 $\mu$m. In the latter choice of re-mixing wavelength range, the green trough region is excluded, and at the same time, a generally high signal at the sensor from atmospheric aerosol scattering is observed. A strong aerosol backscattering signal, again, allows accurate inversion of aerosol optical depth.

Prior to the correlation analysis, all reflectance spectra were convolved to the AVIRIS imaging spectrometer band response as of year 2000. Knowing that the lowest AVIRIS bands show relatively low signal to noise ratios Green and Pavri (2001), bands below 0.42 $\mu$m are not considered in the VIS, rendering the final VIS re-mixing range to 0.42 - 0.50 $\mu$m. Spectral convolution is not expected to have considerable effect on correlation results, since inherent correlations exist between nearby wavelengths for natural surface spectra (Price, 1994). Following the unmixing/re-mixing procedure as defined above, the uncertainty in aerosol optical depth caused by the inaccuracy of approximated VIS surface reflectance needs to be assessed. An average relative deviation of 26.7 % (= $\Delta\rho_s$ in equations (5) and (6)) between real VIS spectrum and re-mixed VIS spectrum could be ascertained, using averaged soil and vegetation spectra as endmembers, and individual soil and vegetation spectra from the region-specific selection as test spectra.

## 5 Application of methods

### *5.1 ARIA*

Application of the ARIA method after figure 3 is now carried out on the basis of the "Topanga" AVIRIS scene. ARIA results are compared to the results as provided by alternative methods for aerosol parameter retrieval. They have been outlined before: dark vegetation and Kaufman's band ratio methods.

As mentioned before, unmixing of the sensor signal has been performed in the SWIR range between 1.97 and 2.38 $\mu$m. In the re-mixing process of $\rho_s$(VIS), the SWIR-VIS correlation of surface reflectance analysis suggested the use of the spectral region between 0.42 and 0.50 $\mu$m. Matching of upward-calculated and sensor spectra worked satisfactorily for maritime and rural aerosol models, with 78 % of SAM-classified pixels useable for aerosol optical depth retrieval. Less matching success could be observed for the urban aerosol model, where only about 60 % of all pre-classified pixels were useable.

### *5.2 Dark targets*

Over land, aerosol parameter inversion was carried out over dark vegetation (DV) targets, for comparison with the ARIA method. For the identification of DV, a combination of band thresholds and a vegetation index was used. Since the normalized difference vegetation index NDVI is not generally applicable to atmospherically distorted image data, as it is itself affected by aerosols, the Atmospherically Resistant Vegetation Index (ARVI) as defined by Kaufman and Tanré (1992) was employed. It is, for a wide range of vegetation types and

atmophseric conditions, on average four times less sensitive to atmospheric effects than the NDVI, and defined by

$$\text{ARVI} = (\rho^*(\text{NIR}) - \rho^*_{rb})/(\rho^*(\text{NIR}) + \rho^*_{rb}) \tag{8}$$

where

$$\rho^*_{rb} = \rho^*_r - \gamma(\rho^*_b - \rho^*_r) \tag{9}$$

with a correction factor $\gamma$. The subscripts $r$ and $b$ denote the red and blue bands, which are positioned at 0.47 $\mu$m (AVIRIS band 11) and 0.66 $\mu$m (33), respectively. The NIR band is chosen at 0.87 $\mu$m (55). Quantities $\rho^*_r$, $\rho^*_b$, and $\rho^*(\text{NIR})$ are already corrected for molecular scattering and absorption analogous to the dark water case. As regards the correction factor $\gamma$, Huete et al. (1997) could show a very good correlation of ARVI and NDVI for a globally representative variation of surface covers with $\gamma = 1$. Also over areas with little green vegetation, the applicability of ARVI with $\gamma = 1$ could be proven (Miura et al., 1998). The latter observation confirms the use of this value for $\gamma$ in this study, as partly low vegetation cover can be expected in the Santa Monica Mountains area in the AVIRIS scene.

According to Kaufman and Tanré (1992), the ARVI threshold is flexibly set such that 5 % of image pixels are included. From this pixel fraction, the semi-fraction with lower reflectance in the NIR band is finally selected as candidate pixels for the dark vegetation method. In the "Topanga" scene, an ARVI threshold of 0.72 was imposed. Once a DV pixel map is obtained, $\rho_s(0.66\mu\text{m})$ is assumed to be $\rho_s^{min} = 0.02$, or $\rho_s^{max} = 0.03$. For both dark target approaches, the uncertainty in the finally retrieved aerosol parameter $\tau_a$ is

calculated analogously to the ARIA method, for a single band. The different assumptions for $\rho_s$ cause an uncertainty in retrieved aerosol optical depth. Referring to equations (5) and (6), ), in the dark target case, $\tau_a^{max}$ and $\tau_a^{min}$ are defined as follows:

$$\tau_a^{max} = f(\rho_s^{min}, \rho_{app}(\lambda_0) + \Delta\rho_{app}(\lambda_0)) \quad \text{and} \tag{10}$$

$$\tau_a^{min} = f(\rho_s^{max}, \rho_{app}(\lambda_0) - \Delta\rho_{app}(\lambda_0)) \ , \tag{11}$$

In the calculation of final aerosol maps, the 0.75 error threshold was used analogously to the ARIA method.

### *5.3 Band ratio*

The band ratio (BR) method was applied according to Kaufman et al. (1997) and the MODIS Algorithm Theoretical Basis Document (Kaufman and Tanré, 1998). For the 2.10 $\mu$m band (AVIRIS band 183), a maximum $\rho_{app}$ threshold of 0.05, and a minimum threshold of 0.005 is imposed, provided that at least 5 % of the pixels in the image are covered that way. Otherwise, the $\rho_{app}$ threshold is increased to 0.1. The minimum threshold should guarantee the exclusion of water pixels. However, in the AVIRIS scene, several water pixels with a high content in suspended matter, mostly close to the shoreline, were erroneously classified as eligible for the band ratio method. For that reason, the additional condition of minimum 2 m terrain height for classified pixels had to be imposed.

The 0.05 reflectance threshold in the SWIR could then be successfully applied. The SWIR/VIS band ratios are applied to approximate the band values at

0.49 $\mu$m (AVIRIS band 13) and 0.66 $\mu$m (33) by the factors of 0.25 and 0.5, respectively. Uncertainties in the retrieved $\tau_a$ were calculated analogously to the ARIA method for two bands in the VIS. Kaufman et al. (1997) gives an absolute uncertainty in the reconstructed band reflectance of 0.006, so total uncertainty in $\rho_s(\lambda)$ is here given by

$$\Delta\rho_s(\lambda) = 0.006 + 0.038\rho_s(\lambda)\,. \tag{12}$$

In the calculation of final aerosol maps, the 0.75 error threshold was used analogously to the ARIA method.

## 6 Results and Discussion

(Insert table 1 about here.)

Aerosol optical depth $\tau_a$ is determined for maritime, rural, and urban aerosol models, for the DV, BR, and ARIA methods. For comparison of the raw inversion results, the statistics of all commonly selected pixels for all methods on an intersection mask yielded mean values $\overline{\tau_a}$, $\overline{\Delta\tau_a}$ and the spatial standard deviation $\sigma(\tau_a)$ calculated for the "Topanga" scene, as well as for the "Valley" and "Urban" subscenes. In the "Topanga" case (table 1), only small relative differences between maritime and rural models can be observed in all categories. This suggests that both models are equally fit to approximate real conditions. Use of the urban model yields values for all categories that stand considerably apart. Absolute aerosol optical depth levels as well as uncertainties are clearly highest, the former exceeding the expected $\tau_a$ of 0.20 by a factor of two.

Maritime and rural results for $\overline{\tau_a}$ in the BR and DV methods are significantly

higher than for the ARIA method. In-scene variations of aerosol optical depth are also lowest for the ARIA method, followed by the other two approaches. The average uncertainty of the retrieved parameter turns out lowest with the DV method for all aerosol models, followed at equal level by the ARIA and BR methods. The uncertainty $\Delta\tau_a^\epsilon$ resulting from the best fit error (cf. equation 7) does not exceed 5 % of the total uncertainty for all methods.

(Insert table 2 about here.)

In the "Valley" subscene of the "Topanga" image (see table 2), aerosol optical depth parameters closely approximate the respective values for the entire scene, and the assessment made previously could be confirmed. The ARIA in-scene variability of $\tau_a$ again is clearly lowest, and the total error approximately at level with the BR method results. The DV method performs best in terms of total uncertainty, probably due to the inversion being done in one spectral band only. The "Urban" subscene evaluation on an intersection mask for all three methods yielded overall higher $\tau_a$ levels for all methods, as expected for this part of the scene (table 3). However, use of the urban aerosol model is not justified even in this subscene, as aerosol optical depth is clearly above the expected level. Total uncertainties of the DV method approximate those for the other methods, indicating a weaker performance of this approach over built-up areas. In-scene variations are again lowest with the ARIA method compared to BR and DV methods.

(Insert table 3 about here.)

Averaging of the raw inversion results on a 25 by 25 pixel mask leads to spatial maps of aerosol optical depth according to step (8) of the proposed ARIA method, and is carried out in the same manner for the BR and DV

method results. Figure 6 shows the results obtained for a rural aerosol model.

(Insert figure 6 about here.)

A better coverage of the land surface can be discerned for the ARIA method, compared to the BR and DV cases. The tendency for higher $\tau_a$ levels in the urban area (easternmost part of map) towards lower values in the mountaineous parts (central and western areas) can be confirmed for ARIA and BR methods. ARIA shows smooth aerosol optical depth for the most part of the scene, with values between 0.14 and 0.20 (blue regions). This is correlated to the existence of strong topography in these areas, and, for the most part, the absence of urban areas. Note the green patch in the centre of the scene that stretches inward to the predominantly blue region: it matches fairly well with an outskirt urban area that extends into a north-south running valley. Isolated patches of very high $\tau_a$ most likely correspond to spurious pixels that have been classified as vegetation or soil in the ARIA procedure, but are strongly mixed with other surface types. Very few pixels are useable in the densely built-up urban area in the south-eastern corner of the scene, where white patches are frequently encountered.

The BR result looks in first approximation similar to the ARIA case, i.e. the distribution of blue and green regions is reproduced. The BR shows stronger inherent variability in both blue and green areas. Less pixels are used by this method, as can be noted from scattered white patches across the scene. Further, more outlying values (red and yellow dots) can be observed, which are most probably not linked to actual variations in aerosol concentration. The DV result appears smoother than the corresponding picture for BR, the blue regions have disappeared, but unexpectedly high $\tau_a$ values (0.45 and

more) can be observed for large eastern and also central parts of the scene. Less of a trend in aerosol optical depth between urban and mountaineous regions is discernible. Figure 7 shows grid-averaged optical depth maps for the "Valley" subscene, again for a rural aerosol model. The smoother spatial variability of the ARIA inversion is reflected in the predominant dark blue shades with relatively few gaps. BR and DV results appear spikier and less spatially contiguous. Aerosol optical depth maps appear very similar for the BR and DV methods in the "Urban" subscene, with scattered spikes (red) and undefined areas (white). These can be explained by poor performance of these methods in the presence of adjacency effects due to bright objects in the urban area.

From above results, maritime and rural aerosol models appear equally fit to describe the actual atmospheric conditions in the "Topanga" scene as well as in both subscenes, despite their different location and expected characteristics. Results for the urban model appear not appropriate for atmospheric characterization in this case, since they exhibit unexpectly high aerosol optical depths and very little valid (in terms of uncertainty level) spatial coverage.

(Insert figure 7 about here.) (Insert figure 8 about here.)

A significant part of the variations in the result of the ARIA method is most probably not due to actual variation of the aerosol regime in the image. Considering maximum $\tau_a$ variations of 0.07 due to topography, this is clearly exceeded in the ARIA results, but also in the results for the BR and DV methods. $\tau_a$ appears conspicuously high (green areas) over mostly urban regions that exhibit many high VIS albedo objects, such as roofs and bright concrete.

## 7 Conclusions

A new method for the retrieval of aerosol parameters over land using imaging spectrometer data has been presented, representing an extension to existing methods for aerosol inversion that are based on single (dark target) or double spectral bands (Kaufman's band ratio). In comparison to band ratio and dark target methods, performance of the ARIA method is encouraging in terms of in-scene smoothness (due to a larger number of pixels used), and comparable uncertainty level in aerosol optical depth while at the same time using more spectral information from the image scene. Especially on a local scale, on the level of subscenes, smoother variation of aerosol optical depth as obtained with the ARIA method in contrast to band ratio and dark vegetation methods becomes particularly apparent. The rural and maritime aerosol models both equally well describe actual aerosol conditions, as derived from this method comparison. Use of the urban aerosol model mostly yielded unreasonable or even no results at all in the analyses. Therefore, it is most likely not adequate for the aerosol regime description in this case study, even for the "Urban" subscene.

Average uncertainties in the ARIA method for aerosol optical depth are comparable to the uncertainties for band ratio and dark target methods. Still, results are affected by the distribution of visibly bright objects, particularly in urban regions. Improbably strong variations of $\tau_a$, that cannot be attributed to terrain height undulation, and are unlikely to reflect true atmospheric conditions, are observed for all methods. The AVIRIS 2000 test imagery, collected between downtown Los Angeles and Point Mugu along the coastline, showed the desired high variation of surface cover, but most probably exhibited a

rather low overall level of aerosol loading, which rendered aerosol parameter inversion independent of surface cover a difficult task.

What is the advantage of more accurate surface reflectance $\rho_s(\lambda)$ spectral sampling, compared to single or double-band-based methods? The dependence of (back-)scattered radiation on wavelength by the Ångström law implies that, in the idealized case of a Junge size distribution and single scattering, two spectral estimates of $\tau_a(\lambda)$ suffice for the spectral description of $\tau_a$ and therefore $\rho_a$ (Liou, 1980). First, the accuracy of approximated $\rho_s(\lambda_o)$ can be improved by simultaneous knowledge of $\rho_s(\lambda_o \pm \Delta\lambda)$ with small $\Delta\lambda$, given high autocorrelation of the surface spectrum. This can be relevant if band $\lambda_o$ is noisy or poorly calibrated. Second, the Ångström law is only an approximation to reality, and higher order $\lambda$-dependence of $\rho_a$ can be of interest.

## 8 Outlook

Our results confirm that the ARIA concept is a further step toward aerosol retrieval and atmospheric correction over land on a pixel basis using high resolution imaging spectroscopy. It shows comparable performance with regard to traditional single or double-band aerosol retrieval methods. Of particular value is the fact that the method does not require *a priori* knowledge, except for the selection of representative endmember spectra from a region-specific selection of spectra, most adequately retrieved from a spectrum database. Until SWIR and VIS high-resolution imaging spectrometer data with global coverage is commonly available, a contribution to the mapping of regional distribution of aerosol parameters has been made. Complementary, the results from this study can be used for regional correction of atmosphere for land cover

analyses.

For the validation of ARIA, the application to imaging spectrometry data is suggested where ground data in form of *in situ* ground reflectance spectra, Sun photometer data (Holben et al., 1998), and/or lidar data is available. In order to circumvent the need for *a priori* endmember choice from a region-specific spectral selection, a number of methods for automated endmember determination has been developed (Tompkins et al., 1997; Winter, 1999). The algorithm by Plaza et al. (2001) appears particularly suited for AVIRIS data. Inclusion of automated endmember determination would represent an elegant extension for the ARIA method, completely removing the need for *a priori* assumptions on endmember spectra.

A sensitivity study of the ARIA result with respect to the choice of unmixing endmembers may further elucidate the mechanisms behind the unmixing/remixing procedure proposed in the ARIA method.

A further step in the inversion process would be the extension of aerosol parameter retrieval to other physical quantities, such as Ångström coefficient or single-scattering albedo. This would allow the determination of the aerosol model also, so far treated separately from the $\tau_a$ inversion. ARIA provides ideal grounds for that, as good spectral VIS coverage is available for the spectral approximation of the aerosol effect.

## 9 Acknowledgements

The authors thank Dar Roberts and Phil Dennison (both University of California Santa Barbara) for providing AVIRIS imagery and surface spectral

data. We are indebted to André Prévôt and Christoph Popp for their help in this project. We gratefully acknowledge financial support from the Swiss National Science Foundation, project 2000-61431.00, and the Paul Scherrer Institut, Villigen, Switzerland.

## List of symbols

| Symbol | Explanation |
|---|---|
| $\rho_a$ | Aerosol optical effect |
| $\rho_{app}$ | Apparent reflectance at sensor level |
| $\rho^*$ | Apparent reflectance at sensor, corrected for molecular scattering contributions |
| $\rho_s$ | Surface reflectance |
| $\tau_a$ | Aerosol optical depth at $\lambda = 0.55$ $\mu$m |
| $V$ | Horizontal visibility |
| $h$ | Terrain height above sea level |
| $\sigma_{e,a}$ | Aerosol extinction coefficient |
| $r_{xy}$ | Pearson's correlation coefficient |
| $\Delta X$ | Absolute error of quantity X |

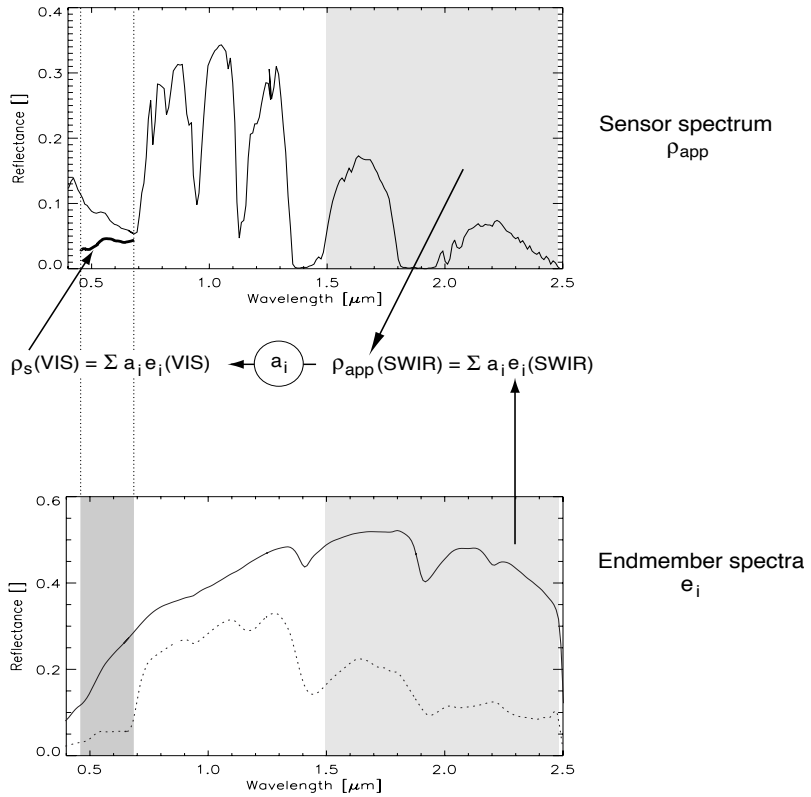


Fig. 1. Principle of $\rho_s$(VIS) approximation by the ARIA method. It is based on spectral unmixing of the sensor spectrum $\rho_{app}$ with appropriate endmembers $e_i$ in the SWIR (light grey), obtaining abundances $a_i$, and subsequent re-mixing of endmembers (dark grey) in the VIS range. The lower panel depicts mean soil (solid line) and vegetation spectra (dashed line).

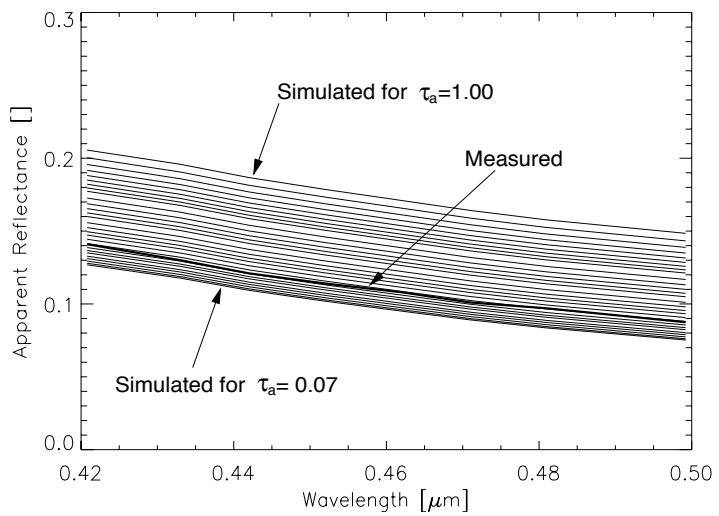


Fig. 2. Simulated at-sensor spectra $\rho_{app}^{sim}$ for variation of $\tau_a$ between 0.07 and 1.00 for maritime aerosol type, based on re-mixed $\rho_s(\lambda)$, compared to measured $\rho_{app}$ at sensor. The VIS range $0.42 - 0.50$ $\mu$m is used for parameter inversion.

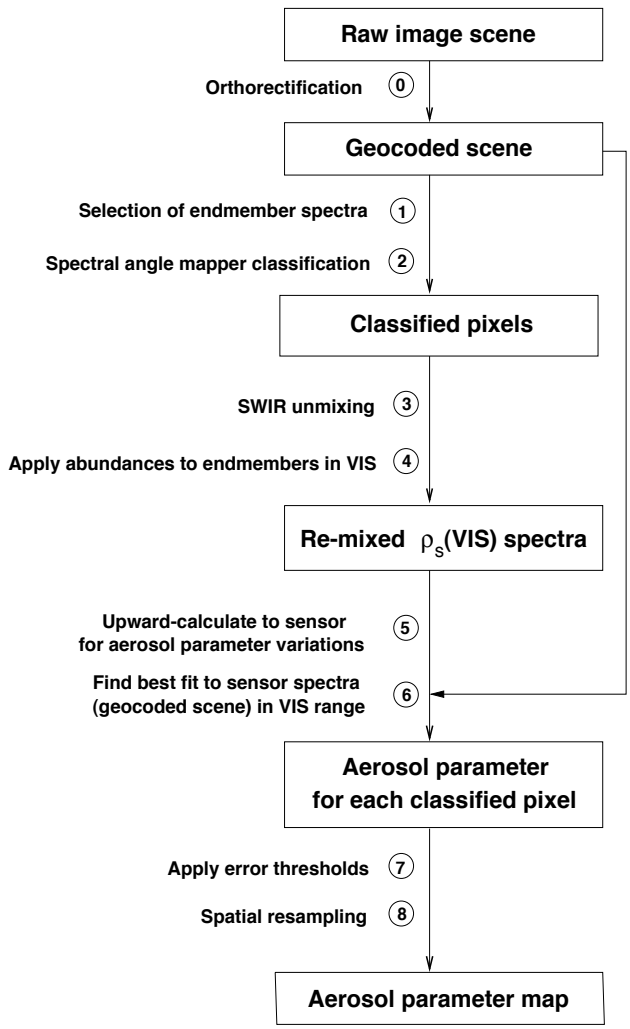


Fig. 3. Implementation schema of the ARIA method.

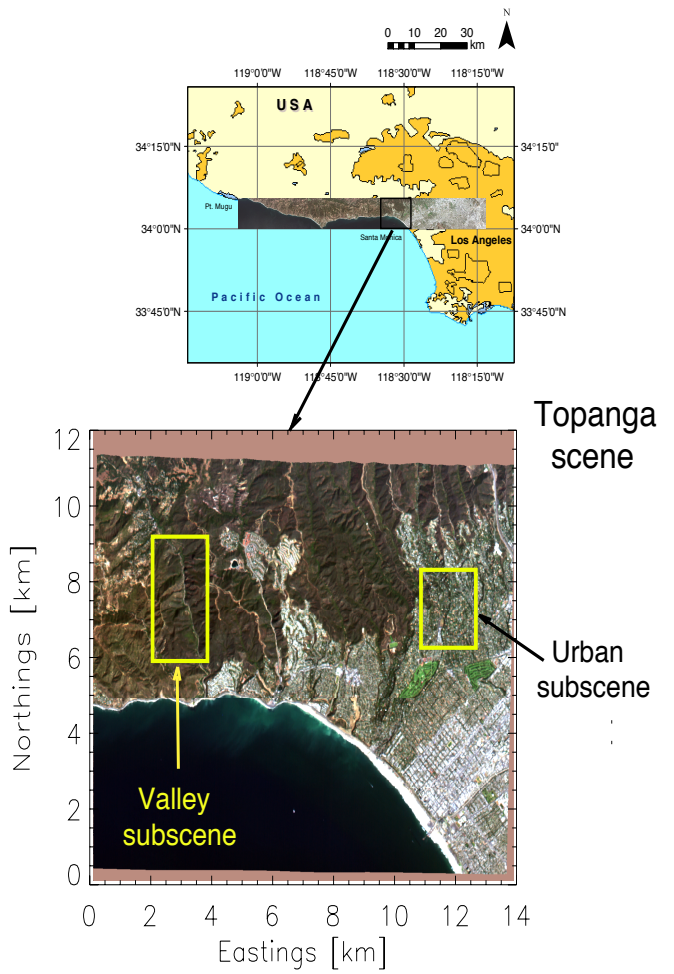


Fig. 4. Location of the AVIRIS scene in the flight line. The zoom-in shows the "Topanga"scene for AVIRIS band 20 (0.56 $\mu$m). Highlighted are the two subscenes "Valley" and "Urban" with characteristic land covers and topography.

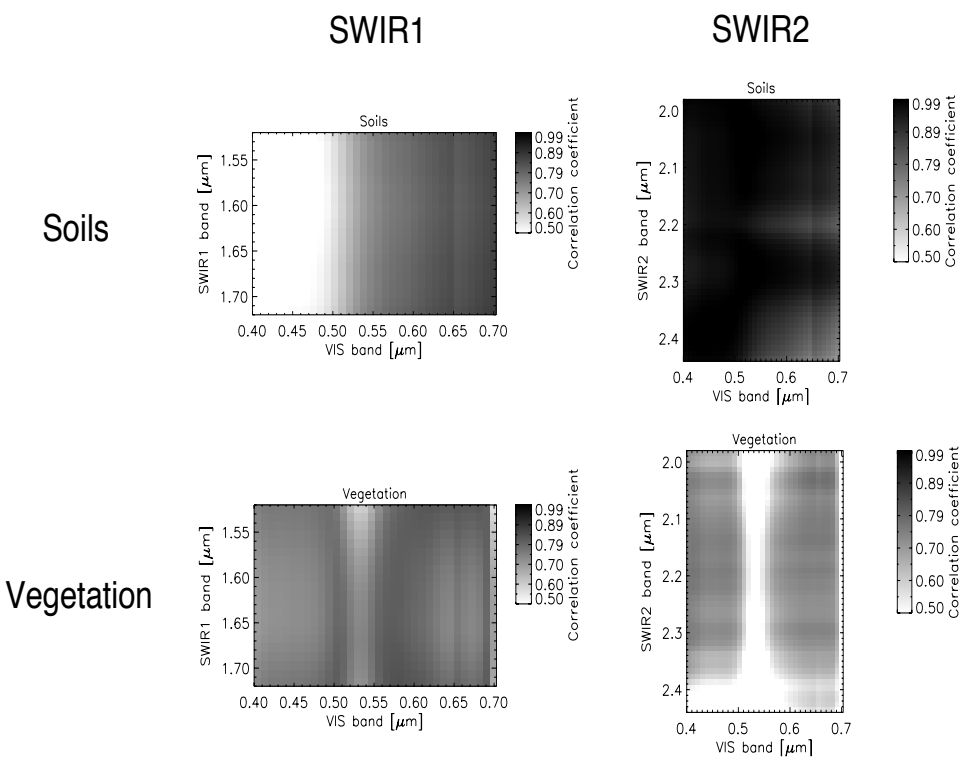


Fig. 5. Correlation of surface reflectance from vegetation and soil in the Santa Monica area, taken from a spectrum database.

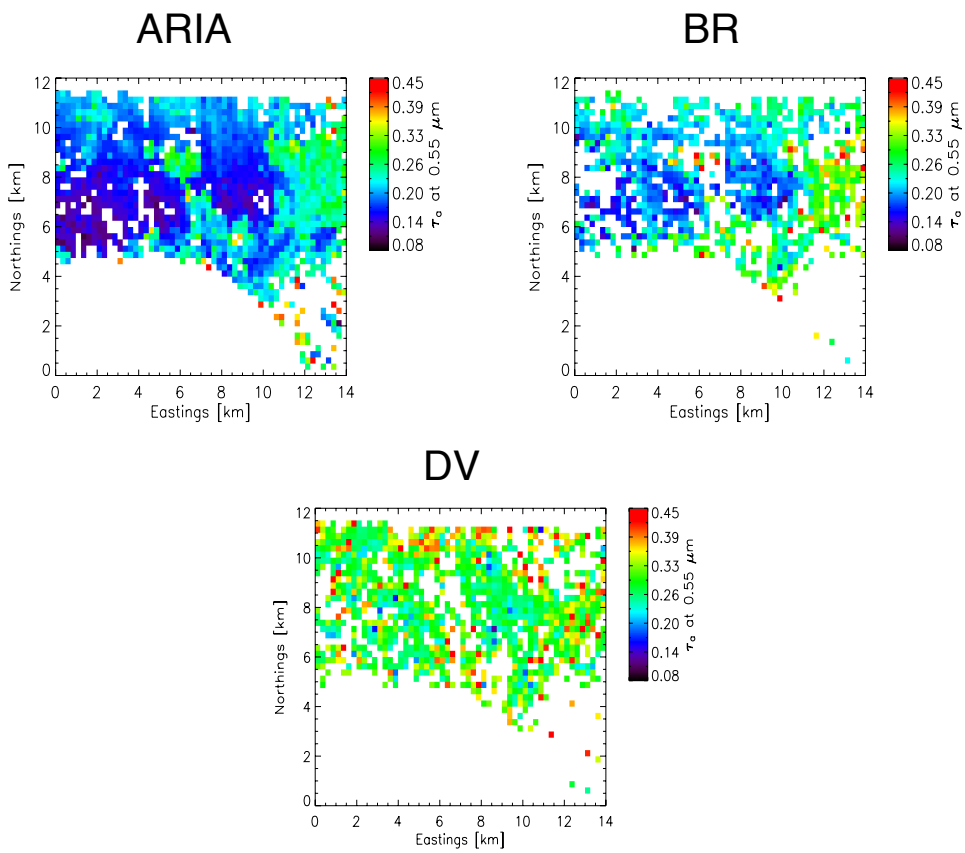


Fig. 6. Examples for spatial mapping results of aerosol optical depth after averaging, using rural aerosol model, for three methods ARIA, band ratio (BR), and dark vegetation (DV) in the "Topanga" scene. White areas denote non-used or out-of-area pixels, or pixels with values that are considered unrealistically high.

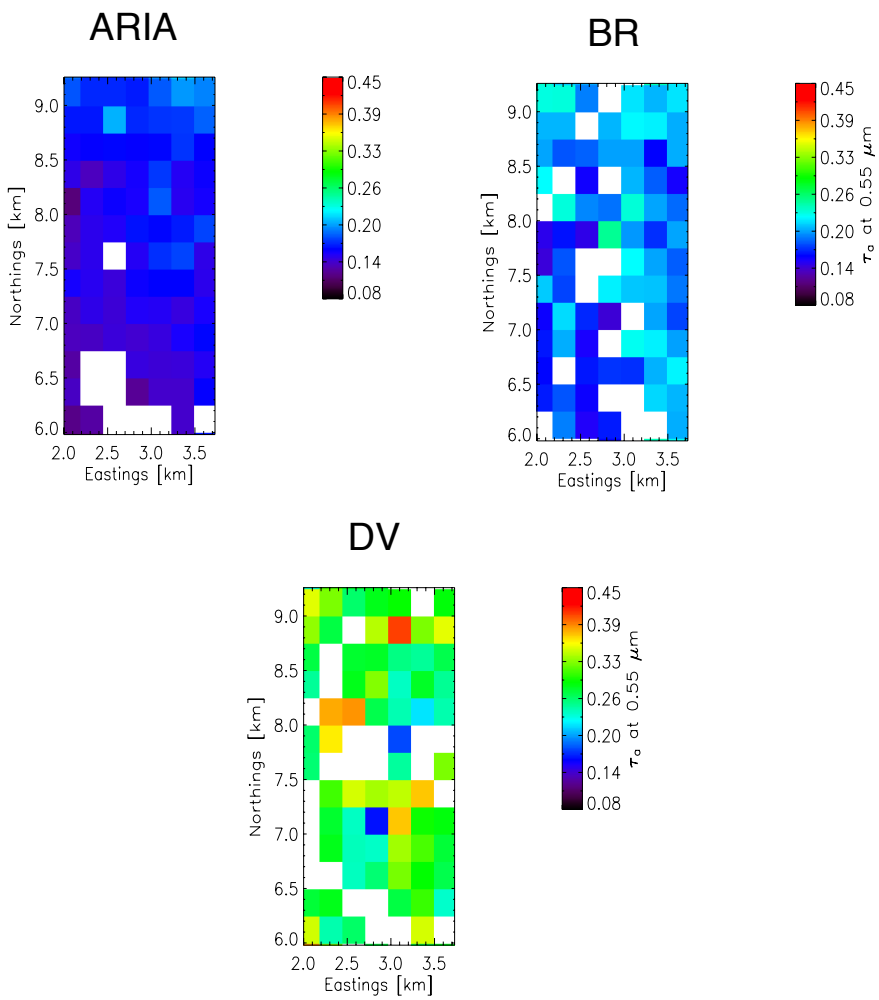


Fig. 7. Examples for spatial mapping results of aerosol optical depth after averaging, using rural aerosol model, for three methods ARIA, band ratio (BR), and dark vegetation (DV) in the "Valley" subscene. White areas denote non-used or out-of-area pixels, or pixels with values that are considered unrealistically high.

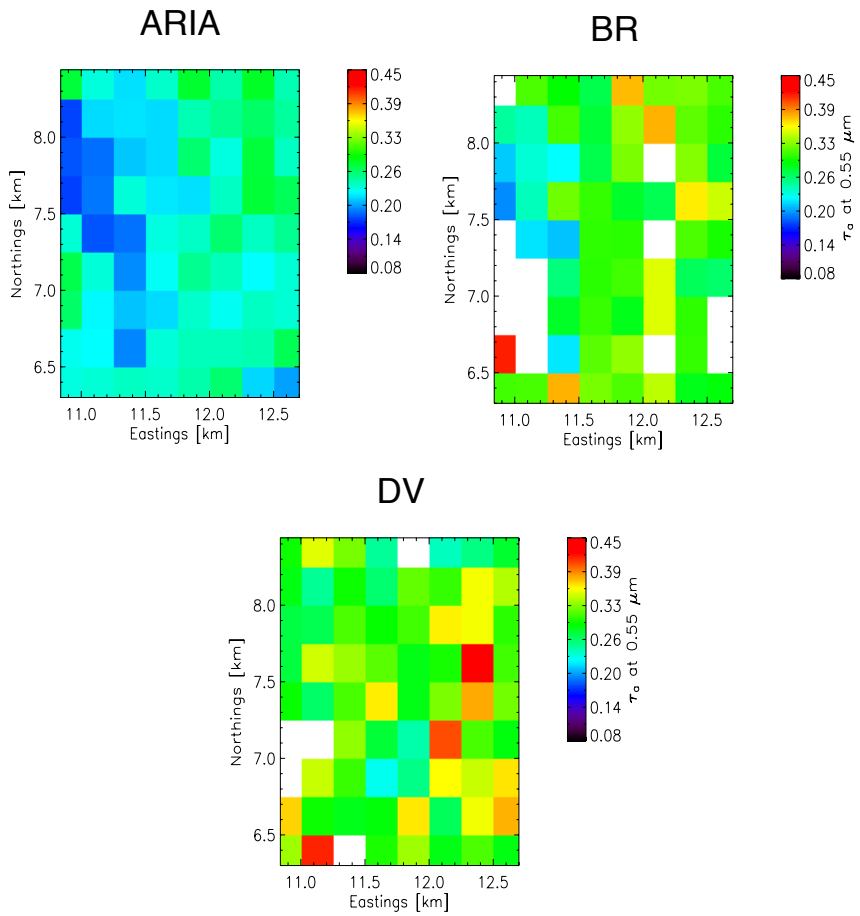


Fig. 8. Examples for spatial mapping results of aerosol optical depth after averaging, using rural aerosol model, for three methods ARIA, band ratio (BR), and dark vegetation (DV) in the "Urban" subscene. White areas denote non-used or out-of-area pixels, or pixels with values that are considered unrealistically high.

| Method | Aerosol | $\overline{\tau_a}$ | $\sigma(\tau_a)$ | $\overline{\Delta\tau_a}$ |
|---|---|---|---|---|
| ARIA | m | 0.21 | 0.03 | 0.09 |
| ARIA | r | 0.18 | 0.03 | 0.09 |
| ARIA | u | 0.44 | 0.11 | 0.29 |
| BR | m | 0.24 | 0.06 | 0.09 |
| BR | r | 0.23 | 0.06 | 0.10 |
| BR | u | 0.56 | 0.22 | 0.32 |
| DV | m | 0.25 | 0.06 | 0.05 |
| DV | r | 0.26 | 0.07 | 0.05 |
| DV | u | 0.51 | 0.15 | 0.08 |

Table 1

"Topanga" scene aerosol mapping results obtained with ARIA, band ratio (BR), and dark target methods (DV), using maritime (m), rural (r), and urban (u) aerosol models, evaluated on an intersection mask.

| Method | Aerosol | $\overline{\tau_a}$ | $\sigma(\tau_a)$ | $\overline{\Delta\tau_a}$ |
|---|---|---|---|---|
| ARIA | m | 0.18 | 0.01 | 0.10 |
| ARIA | r | 0.16 | 0.01 | 0.09 |
| ARIA | u | 0.35 | 0.05 | 0.27 |
| BR | m | 0.24 | 0.05 | 0.10 |
| BR | r | 0.23 | 0.05 | 0.10 |
| BR | u | 0.54 | 0.20 | 0.35 |
| DV | m | 0.25 | 0.07 | 0.06 |
| DV | r | 0.26 | 0.07 | 0.06 |
| DV | u | 0.49 | 0.17 | 0.07 |

Table 2

"Valley" subscene aerosol mapping results obtained with ARIA, band ratio (BR), and dark target methods (DV), using maritime (m), rural (r), and urban (u) aerosol models, evaluated on an intersection mask.

| Method | Aerosol | $\overline{\tau_a}$ | $\sigma(\tau_a)$ | $\overline{\Delta\tau_a}$ |
|---|---|---|---|---|
| ARIA | m | 0.24 | 0.03 | 0.10 |
| ARIA | r | 0.22 | 0.03 | 0.09 |
| ARIA | u | 0.54 | 0.10 | 0.30 |
| BR | m | 0.28 | 0.06 | 0.10 |
| BR | r | 0.27 | 0.06 | 0.11 |
| BR | u | 0.71 | 0.24 | 0.37 |
| DV | m | 0.28 | 0.08 | 0.08 |
| DV | r | 0.29 | 0.08 | 0.08 |
| DV | u | 0.52 | 0.15 | 0.08 |

Table 3

"Urban" subscene aerosol mapping results obtained with ARIA, band ratio (BR), and dark target methods (DV), using maritime (m), rural (r), and urban (u) aerosol models, evaluated on an intersection mask.

## References


ASNER, G. and LOBELL, D. (2000). A biogeophysical approach for automated SWIR unmixing of soils and vegetation. Remote Sensing of Environment, 74, 99–112.

BERK, A., BERNSTEIN, L., and ROBERTSON, D. (1989). MODTRAN: a moderate resolution model for LOWTRAN7. Technical report, Spectral Sciences Inc., Burlington, Massachusetts, USA, 38 pp.

BOJINSKI, S., SCHAEPMAN, M., SCHLÄPFER, D., and ITTEN, K. (2003). SPECCHIO: a spectrum database for remote sensing applications. Computers & Geosciences, 29(1), 27–38.

CHOMKO, R. and GORDON, H. (1998). Atmospheric correction of ocean color imagery: use of the Junge power-law aerosol size distribution with variable refractive index to handle aerosol absorption. Applied Optics, 37(24), 5560–5572.

FRASER, R. (1976). Satellite measurements of mass of Saharan dust in the atmosphere. Applied Optics, 15, 2471–2479.

GAO, B., MONTES, M., AHMAD, Z., and DAVIS, C. (2000). Atmospheric correction algorithm for hyperspectral remote sensing of ocean color from space. Applied Optics, 39(6), 887–896.

GORDON, H. (1978). Removal of atmospheric effects from satellite imagery of the oceans. Applied Optics, 17(10), 1631–1636.

GORDON, H. and WANG, M. (1994). Retrieval of water-leaving radiance and aerosol optical thickness over the oceans with SeaWiFS: a preliminary algorithm. Applied Optics, 33(3), 443–452.

GREEN, R., EASTWOOD, M., SARTURE, C., CHRIEN, T., ARONSSON, M., CHIPPENDALE, B., FAUST, J., PAVRI, B., CHOVIT, C., SOLIS,

M., OLAH, M., and WILLIAMS, O. (1998). Imaging spectroscopy and the airborne visible/infrared imaging spectrometer (AVIRIS). Remote Sensing of Environment, 65, 227–248.

GREEN, R. and PAVRI, B. (2001). AVIRIS inflight calibration experiment measurements, analyses, and results in 2000. In Summaries of the Tenth Annual JPL Airborne Geoscience Workshop, volume 1, Pasadena, California, USA, pp. 205–218.

HOLBEN, B., ECK, T., SLUTSKER, I., TANRÉ, D., BUIS, J., SETZER, A., VERMOTE, E., REAGAN, J., KAUFMAN, Y., NAKAJIMA, T., LAVENU, F., JANKOWIAK, I., and SMIRNOV, A. (1998). AERONET - a federated instrument network and data archive for aerosol characterization. Remote Sensing of Environment, 66, 1–16.

HUETE, A., LIU, H., BATCHILY, K., and VAN LEEUWEN, W. (1997). A comparison of vegetation indices over a global set of TM images for EOS-MODIS. Remote Sensing of Environment, 59, 440–451.

ISAKOV, V., FEIND, R., VASILYEV, O., and WELCH, R. (1996). Retrieval of aerosol spectral optical thickness from AVIRIS data. International Journal of Remote Sensing, 17(11), 2165–2184.

KARNIELI, A., KAUFMAN, Y., REMER, L., and WALD, A. (2001). AFRI - aerosol free vegetation index. Remote Sensing of Environment, 77, 10–21.

KAUFMAN, Y. and SENDRA, C. (1988). Algorithm for automatic atmospheric corrections to visible and near-IR satellite imagery. International Journal of Remote Sensing, 9(8), 1357–1381.

KAUFMAN, Y. and TANRÉ, D. (1992). Atmospherically resistant vegetation index (ARVI) for EOS-MODIS. IEEE Transactions on Geoscience and Remote Sensing, 30(2), 261–270.

KAUFMAN, Y. and TANRÉ, D. (1998). Algorithm for remote sensing of

tropospheric aerosols from MODIS. NASA Goddard Space Flight Center, Greenbelt, Maryland, USA, 85 pp.

KAUFMAN, Y., TANRÉ, D., and BOUCHER, O. (2002). A satellite view of aerosols in the climate system. Nature, 419, 215–223.

KAUFMAN, Y., WALD, A., REMER, L., GAO, B., LI, R., and FLYNN, L. (1997). The MODIS 2.1-$\mu$m channel-correlation with visible reflectance for use in remote sensing of aerosol. IEEE Transactions on Geoscience and Remote Sensing, 35(5), 1286–1297.

KING, M., KAUFMAN, Y., MENZEL, W., and TANRÉ, D. (1992). Remote sensing of cloud, aerosol, and water vapor properties from the moderate resolution imaging spectrometer (MODIS). IEEE Transactions on Geoscience and Remote Sensing, 30(1), 2–27.

LEROY, M., DEUZÉ, J. L., BRÉON, F. M., HAUTECOEUR, O., HERMAN, M., BURIEZ, J. C., TANRÉ, D., BOUFFIÈS, S., CHAZETTE, P., and ROUJEAN, J. L. (1997). Retrieval of atmospheric properties and surface bidirectional reflectances over land from POLDER/ADEOS. Journal of Geophysical Research, 102(D14), 17023–17037.

LIOU, K.-N. (1980). An Introduction to Atmospheric Radiation. Academic Press, New York, New York, USA, 392 pp.

MARTONCHIK, J., DINER, D., KAHN, R., ACKERMAN, T., VERSTRAETE, M., PINTY, B., and GORDON, H. (1998). Techniques for the retrieval of aerosol properties over land and ocean using multiangle imagery. IEEE Transactions on Geoscience and Remote Sensing, 36(4), 1212–1227.

MIURA, T., HUETE, A., VAN LEEUWEN, W., and DIDAN, K. (1998). Vegetation detection through smoke-filled AVIRIS images: an assessment using MODIS band passes. Journal of Geophysical Research, 103(D24), 32001–32011.

PLAZA, A., MARTINEZ, P., GUALTIERI, J., and PEREZ, R. (2001). Spatial/spectral identification of endmembers from AVIRIS data using mathematical morphology. In Summaries of the Tenth Annual JPL Airborne Geoscience Workshop, volume 1, Pasadena, California, USA, pp. 309–319.

PRESS, W., TEUKOLSKY, S., VETTERLING, W., and FLANNERY, B. (1992). Numerical Recipes in C. Cambridge University Press, Cambridge, UK, 2nd edition, 994 pp.

PRICE, J. (1994). Band selection procedure for multispectral scanners. Applied Optics, 33(15), 3281–3288.

RICHARDS, J. and JIA, X. (1999). Remote Sensing Digital Image Analysis. Springer-Verlag, Berlin, Germany, 3rd edition, 363 pp.

RICHTER, R. (1996). A spatially adaptive fast atmospheric correction algorithm. International Journal of Remote Sensing, 17(6), 1201–1214.

RICHTER, R. and SCHLÄPFER, D. (2002). Geo-atmospheric processing of airborne imaging spectrometry data. Part 2: atmospheric/topographic correction. International Journal of Remote Sensing, 23(13), 2631–2649.

ROBERTS, D., GARDNER, M., CHURCH, R., USTIN, S., SCHEER, S., and GREEN, R. (1998). Mapping chaparral in the Santa Monica Mountains using multiple endmember spectral mixture models. Remote Sensing of Environment, 65(3), 267–279.

SCHLÄPFER, D. and RICHTER, R. (2002). Geo-atmospheric processing of airborne imaging spectrometry data. Part 1: parametric orthorectification. International Journal of Remote Sensing, 23(13), 2609–2630.

SEINFELD, J. and PANDIS, S. (1998). Atmospheric Chemistry and Physics. Wiley, New York, New York, USA, 1326 pp.

SHETTLE, E. and FENN, R. (1979). Models for the aerosols of the lower atmosphere and the effects of humidity variations on their optical proper-

ties. Technical Report AFGL-TR-79-0214, Air Force Geophysics Laboratory, Hanscom AFB, Massachusetts, USA, 94 pp.

TANRÉ, D., HERMAN, M., and DESCHAMPS, P. (1983). Influence of the atmosphere on space measurements of directional properties. Applied Optics, 22(5), 733–741.

Tanré, D., Herman, M., and Mattoo, S. (1997). Remote sensing of aerosol properties over oceans using the MODIS/EOS spectral radiances. Journal of Geophysical Research, 102(D14), 16971–16988.

TOMPKINS, S., MUSTARD, J., PIETERS, C., and FORSYTH, D. (1997). Optimization of endmembers for spectral mixture analysis. Remote Sensing of Environment, 59, 472–489.

VEEFKIND, J., DE LEEUW, G., STAMMES, P., and KOELJEMEIER, R. (2000). Regional distribution of aerosol over land derived from ATSR-2 and GOME. Remote Sensing of Environment, 74, 377–386.

WINTER, M. (1999). N-FINDR: an algorithm for fast autonomous spectral endmember determination in hyperspectral data. In SPIE Imaging Spectrometry V, volume 3753, Bellingham, Washington, USA, pp. 266-275.